energies

MDPI

Article

High-Efficiency Power Cycles for Particle-Based Concentrating Solar Power Plants: Thermodynamic Optimization and Critical Comparison

Miguel Angel Reyes-Belmonte [1,*] and Francesco Rovense [2,*]

[1] Department of Chemical, Energy and Mechanical Technology, Rey Juan Carlos University, Calle Tulipán, 28933 Móstoles, Madrid, Spain
[2] Laboratorio Energia e Ambiente Piacenza, LEAP s.c.a.r.l., Via Nino Bixio, 27/C, 29121 Piacenza, Italy
* Correspondence: miguelangel.reyes@urjc.es (M.A.R.-B.); francesco.rovense@polimi.it (F.R.)

Abstract: This paper investigates and compares several highly efficient thermodynamic cycles that are suitable for coupling with particle-in-tube fluidized-bed solar receiver technology. In such a receiver, high-temperature particles are used as both a heat transfer fluid and a storage medium. A dense particle suspension (DPS) is created through an upward bubbling fluidized-bed (UBFB) flow inside the receiver tubes, which constitutes the "particle-in-tube" solar receiver concept. Reaching higher temperatures is seen as a key factor for future cost reductions in the solar plant, as this leads to both higher power conversion efficiency and increased energy storage density. Three advanced thermodynamic cycles are analyzed in this work: the supercritical steam Rankine cycle (s-steam), supercritical carbon dioxide cycle (s-CO_2) and integrated solar combined cycle (ISCC). For each one, 100% solar contribution, which is considered the total thermal input to the power cycle, can be satisfied by the solar particle receiver. The main findings show that the s-CO_2 cycle is the most suitable thermodynamic cycle for the DPS solar plant, exhibiting a net cycle efficiency above 50% for a moderate temperature range (680–730 °C). For the other advanced power cycles, 45.35% net efficiency can be achieved for the s-steam case, while the efficiency of the ISCC configuration is limited to 45.23% for the solar-only operation mode.

Keywords: power cycles; particle receivers; thermodynamic optimization; solar energy

check for updates

Citation: Reyes-Belmonte, M.A.; Rovense, F. High-Efficiency Power Cycles for Particle-Based Concentrating Solar Power Plants: Thermodynamic Optimization and Critical Comparison. *Energies* **2022**, *15*, 8579. https://doi.org/10.3390/en15228579

Academic Editors: Lyes Bennamoun and Eric Hu

Received: 30 September 2022
Accepted: 14 November 2022
Published: 16 November 2022

Publisher's Note: MDPI stays neutral with regard to jurisdictional claims in published maps and institutional affiliations.

Copyright: © 2022 by the authors. Licensee MDPI, Basel, Switzerland. This article is an open access article distributed under the terms and conditions of the Creative Commons Attribution (CC BY) license (https://creativecommons.org/licenses/by/4.0/).

1. Introduction

Achieving global net-zero emissions by 2050 and limiting the temperature rise to below 1.5 °C have become the main goals for scientists around the world [1]. To do this, it is necessary to accelerate the process of reducing carbon emissions, reducing deforestation, accelerating the transition to electric vehicles and encouraging investment in renewable energy technologies to increase efficiency and operational flexibility [2]. Several actions have been taken by countries around the world, and among these, the European Green Deal is the transformation plan of the European economy for a sustainable future [3]. It aims to reduce greenhouse gas emissions by at least 55% by 2030 compared to 1990 levels and to become a net-zero-emission, sustainable and resilient economy by 2050. The penetration of renewable energy sources (RES) in distributed electricity generation plays a fundamental role in achieving the objectives set by the European Union.

In this context, concentrating solar power (CSP) is seen as one of the most promising technologies for electricity production for the coming decades compared to other intermittent renewable electricity sources, such as wind and photovoltaics [4]. Amongst the reasons for this, its reliability and flexibility stand out. However, the key point of the technology is that its operation is not limited to when the sun is shining when integrated with thermal energy storage (TES) systems [5]. Furthermore, the water requirements of solar plants are reduced when coupled to dry-cooling systems [6]. Cost reductions attained

by means of other renewable energy sources are forcing CSP developers to move a step further in seeking technology cost reductions [7]. Among cost reduction actions, a higher operating temperature is considered a key factor for the future of CSP technologies, as high temperatures lead to both higher power conversion efficiencies and increased energy storage densities [8]. Molten-salt technology has been proven successful when coupled with subcritical Rankine cycles in solar tower applications [9,10]. However, the operating temperature of commercial molten-salt power plants is limited to 565 °C, which limits conversion efficiency. On the other hand, direct steam CSP generation plants can run at 585 °C, but they are not capable of efficient thermal energy storage, which is key for the deployment of CSP technologies [11]. The use of novel heat transfer fluids (HTFs) enables reaching operating temperatures above 550 °C on the solar receiver, which opens the opportunity to explore innovative thermodynamic cycles with higher conversion efficiency [12] as well as facilitate massive thermal energy storage.

In the case of a particle-based solar central receiver, a flexible plant layout and a high-temperature TES system provide a suitable platform for the integration of advanced thermodynamic power cycles. In addition to the higher temperature of the HTF and the consequently improved thermodynamic power cycle efficiency, using a dense particle suspension (DPS) exhibits many other benefits for CSP applications. For instance, no operating temperature constraints appear (no freezing risks or thermal degradation), and particles are not dangerous or toxic and are cheap and abundant with a high energy density and a high average heat transfer coefficient (above 2000 W/m^2K [13]).

One of the main goals for the next generation of CSP plants is to design systems with rated sun-to-electricity efficiencies close to 30%, as requested by the SunShot initiative [14], compared to the 25% efficiency of state-of-the-art molten-salt tower technology [15]. Novel HTFs allowing for high receiver temperatures will pave the way for future solar power plants coupled to advanced thermodynamic cycles with a conversion efficiency approaching or even exceeding 50% [16].

In this sense, using air as a working fluid for the unfired closed Brayton cycle with particle-based TES has exhibited a net efficiency of 42% at 850 °C [17–19], while supercritical and ultra-supercritical steam Rankine cycles have proven efficiencies in the range of 45% up to 48% [20]. Supercritical CO_2 (s-CO_2) Brayton cycles have a reported cycle efficiency in the vicinity of 50% for different power plant schemes [21], including the particle-based solar central receiver [22]. The integrated solar combined cycle (ISCC) coupled to a particle-based solar central receiver and particle TES proved its ability to reach 49% power plant net efficiency operating at 800 °C in a multi-tower layout arrangement [23]. Based on the abovementioned research works, further discussion is required when using particle-based solar receivers to elucidate which thermodynamic cycle is best coupled with this CSP technology.

In this context, this paper summarizes the main findings and conclusions on a power plant layout comparison for the CSP application when using DPS as a heat transfer fluid and thermal energy storage at operating temperatures above 750 °C [24]. Three advanced power cycle layouts are discussed below: the supercritical Rankine cycle, supercritical CO_2 cycle and integrated solar combined cycle. In the first part of the manuscript, the power plant's general layout and the solving methodology from the existing literature are described, along with key performance indicators considered for comparison purposes. In Section 3, the simulation results of thermodynamic cycles are presented. Section 4 is devoted to the results' discussion, while Section 5 summarizes the paper's main conclusions.

2. Materials and Methods

Figure 1 sketches the particle-based central receiver solar power plant concept with a TES system coupled to a generic power cycle. The main components of the power plant are the solar field (heliostats), the central particle receiver, the hot and cold particle storage tanks, the power block and a series of heat exchangers allowing the thermal energy from the receiver heat transfer fluid (HTF) to be passed to the power cycle working transfer fluid.

The solar power plant includes a particle transportation system from the solar receiver to the storage tanks and, from there, to the heat exchanger network. This architecture is like that of molten-salt CSP plants, where molten salts have been replaced by a DPS HTF.

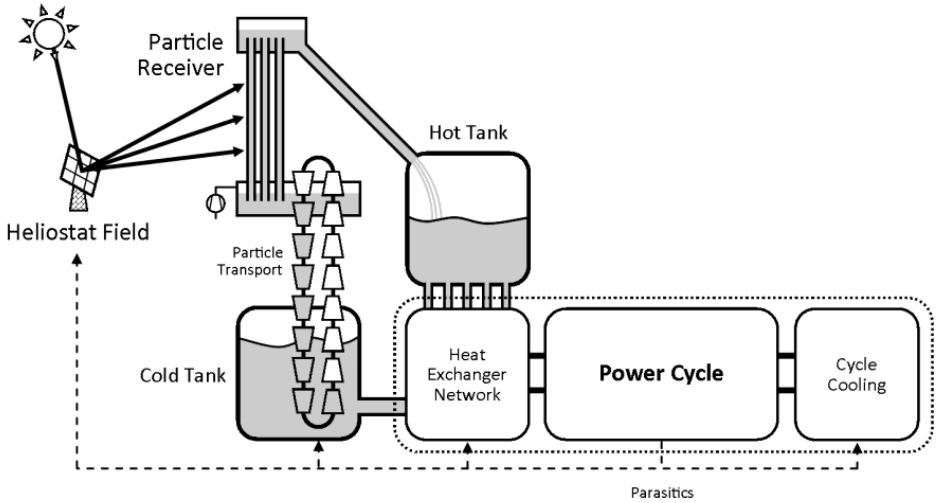


Figure 1. Concentrating solar power plant layout [20].

As illustrated in Figure 1, the solar receiver absorbs concentrated solar radiation that is reflected by the heliostat field and transfers this heat to upward-moving fluidized particles inside the receiver tubes [25]. Hot particles are later stored in a hot storage tank that feeds a series of fluidized-bed heat exchangers. The heat exchanger network transfers the heat from particles to the working fluid when required. Based on the plant's flexible architecture, different working fluids can be considered, such as air, helium, s-CO_2 or steam [15].

The thermodynamic modeling methodology is based on an in-house MATLAB tool for the solar plant component design, steady-state simulations and results processing [25]. Component design optimization is addressed in a backward direction by setting the electricity output of the power block while considering solar receiver design constraints (Figure 2).

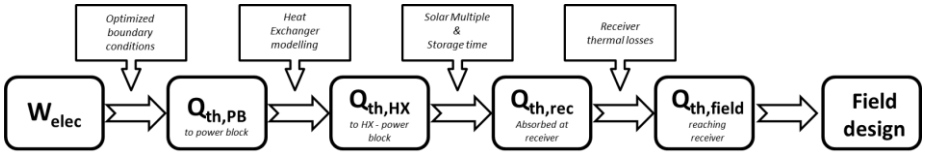


Figure 2. Flowchart of the CSP plant design methodology.

Setting the electricity power output as a design criterion allows for power block boundary condition optimization based on maximizing the energy conversion efficiency and for determining the required thermal input power. After that, the thermal power that is required from the heat transfer fluid loop can be determined according to the heat exchangers' thermal performance. That power, multiplied by the solar multiple, represents the net thermal power absorbed inside the receiver. The power that is required from the solar field and that is considered for heliostat field design considers both the absorbed power inside the solar receiver and the thermal power losses due to radiation and convective mechanisms. The sun-to-electricity efficiency of the plant (η_{S2E}) can be derived by considering all of the efficiencies involved in the energy balance problem, as shown by Equation (1).

$$\eta_{S2E} = \eta_{hel} \cdot \eta_{rec} \cdot \eta_{HTX} \cdot \eta_{cycle} \quad (1)$$

where η_{cycle} represents the net power cycle efficiency, which is the output to be maximized in this targeted function, η_{HTX} stands for the heat exchanger network efficiency connecting the solar loop to the power block [26], η_{rec} represents the central receiver thermal efficiency, and η_{hel} indicates the efficiency of the solar field.

A detailed model description and the validation of the abovementioned components can be found in [27] for the solar receiver modeling equations, in [25] for receiver design methodology, in [28] for heat exchanger modeling equations, in [26] for its design methodology, in [29] for the detailed modeling of the supercritical steam Rankine cycle and in [15] for details on s-CO_2 and ISCC. In this work, previously validated numerical models, resolution and optimization methodology were applied to optimize and compare the performance of several advanced power cycles coupled to the particle-based solar central receiver. In this sense, the technology trends of CSP systems are aligned with high-efficiency power cycles, the use of a new HTF and the development of low-cost thermal energy storage systems to achieve higher solar-to-electricity efficiency while lowering the Levelized Cost of Electricity. Within that frame, innovative supercritical power cycles and integrated solar combined cycle technologies are proposed in this analysis to achieve the 50% net cycle efficiency goal for future third-generation (Gen3) CSP plants [14]. As established in the "Gen3 CSP Roadmap" [16], dense particle suspensions in the solar receiver are seen as one of the most promising technologies enabling higher operating temperatures. Existing particle technologies in industrial applications, including their storage and transportation, can pave the way for particle-based CSP plant development. Table 1 gathers the principal modeling assumptions for the proposed power cycles.

Table 1. Assumptions for power cycle modeling.

Parameter	Unit	S-Steam	S-CO_2	ISCC
Power plant nameplate capacity	MW	150	50	150
Receiver outlet temperature	°C	650	700–750	800
Target net cycle efficiency	%	>45	50	50
Condenser type	-	dry	wet	dry

As can be observed, increasing the working temperature level is considered for each power cycle according to realistic particle-based central receiver designs [30] and power cycles' state-of-the-art. Due to the concentrating solar power plant application, dry condensing scenarios are preferable whenever possible.

3. Results

The supercritical steam Rankine cycle, supercritical carbon dioxide cycle and integrated solar combined power cycle configurations and working conditions were optimized for coupling with the particle-based solar receiver.

3.1. Supercritical Rankine Cycle (S-Steam)

The critical conditions for a water stand at 220 bar and 374 °C with a turbine reheating plant layout were considered to maximize the power cycle efficiency. Typically, an optimal reheating pressure of around one-third of the superheated steam pressure is considered for reheated steam cycles [31]. Table 2 summarizes the boundary conditions for modeling the supercritical steam Rankine cycle layout shown in Figure 3 [32], where five steam extractions were considered for feedwater chain preheating to reduce the heat added for steam generation.

Table 2. Supercritical Rankine cycle components' efficiency.

Parameter	Unit	Value
High-pressure turbine isentropic efficiency	%	91
Low-pressure turbine isentropic efficiency	%	91
Pump efficiency	%	85
Condenser fan mechanical efficiency	%	75
Reheating pressure losses	bar	5
Condenser ΔT (dry)	°C	15
Ambient temperature	°C	25

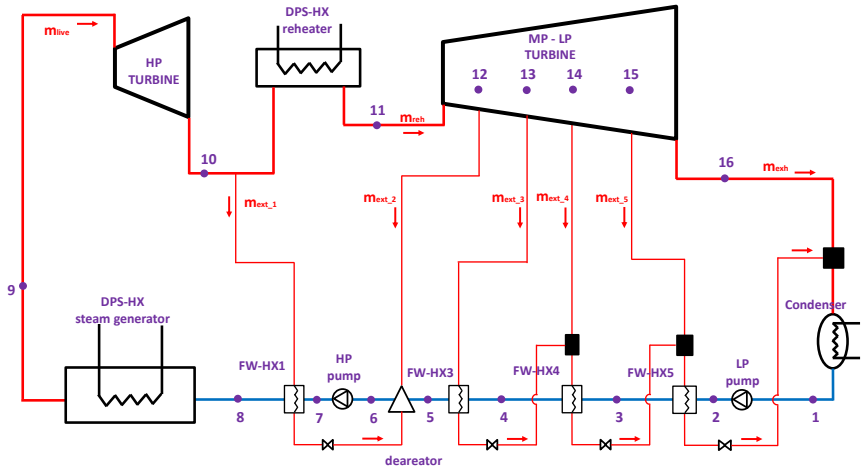


Figure 3. Supercritical steam Rankine cycle layout: HX (Heat exchanger), HP (High Pressure), MP (Medium pressure), LP (Low Pressure), FW (Feedwater preheating chain), DPS (Dense Particles Suspension).

Different working conditions of the pressure and temperature levels for superheated steam, reheated steam and the condenser were analyzed when seeking maximum power cycle efficiency. For the sake of simplicity, two optimized cases are summarized in Table 3 that correspond to two different temperature levels at the condenser (60 °C and 50 °C). Reducing the steam condensing temperature from 60 °C to 50 °C translates into the higher power consumption of the dry-cooling fan, as can be observed in Table 3 for optimized Case 2. This is due to the lower temperature difference between the cooling source (ambient air) and the condensing steam.

It is also true that reducing the steam condensing temperature allows for higher low-pressure turbine power extraction based on the higher enthalpy change of the exhaust steam. However, the steam quality significantly decreases from 95% to 90% at the last turbine stage. A minimum steam quality criterion of 90% is considered from a practical point of view to avoid excessive water droplet formation and consequent turbine blade erosion. Although it is desirable to keep the condenser pressure as low as possible, even if that means more moisture (and erosion), the increase in the parasitic losses of the dry-cooling fans will have excessive negative effects on the thermodynamic optimization of the power cycle, as is shown later in Figure 6.

In addition to a lower condensing temperature, optimized Case 2 is also fed by a higher superheated steam temperature (620 °C). In both simulated cases, a maximum pressure of 285 bar was considered, which is a reasonable value for state-of-the-art supercritical one-through steam generators [33]. Figure 4 summarizes the detailed temperature and enthalpy evolution for both optimized cases; Figure 4 (top) sketches the T-s diagram while Figure 4 (bottom) shows the h-s diagram for superheated steam conditions of 600 °C (left) and 620 °C (right), respectively.

Table 3. Optimized cases for supercritical Rankine cycle (dry cooling).

Parameter	Unit	Case 1	Case 2
Receiver outlet temperature	°C	650	650
Superheated steam temperature	°C	600	620
Reheated steam temperature	°C	620	620
Condensing temperature	°C	60	50
Superheated steam pressure	bar	285	285
Water inlet temperature to the steam generator (calculated)	°C	286.7	317.8
Reheated steam pressure	bar	65	95
Superheated steam mass flow	kg/s	124.01	132.18
Reheated steam mass flow	kg/s	112.38	115.31
Condenser steam mass flow	kg/s	104.43	105.34
First steam extraction mass flow	kg/s	11.63	16.87
Second steam extraction mass flow	kg/s	7.94	9.97
Third steam extraction mass flow	kg/s	8.74	10.60
Fourth steam extraction mass flow	kg/s	7.76	8.95
Fifth steam extraction mass flow	kg/s	6.07	6.94
steam quality	%	95	90
Nameplate capacity	MW_e	150	150
HP net power produced	MW_e	45.63	39.2
LP net power produced	MW_e	113.57	121.3
Feedwater pump consumption	MW_e	4.53	4.74
Circulating pump consumption	MW_e	0.46	0.62
Condensing pump consumption	MW_e	0.35	0.49
Condenser fan consumption	MW_e	3.68	4.47
Gross cycle efficiency	%	46.01	47.90
Net cycle efficiency	%	43.82	45.35

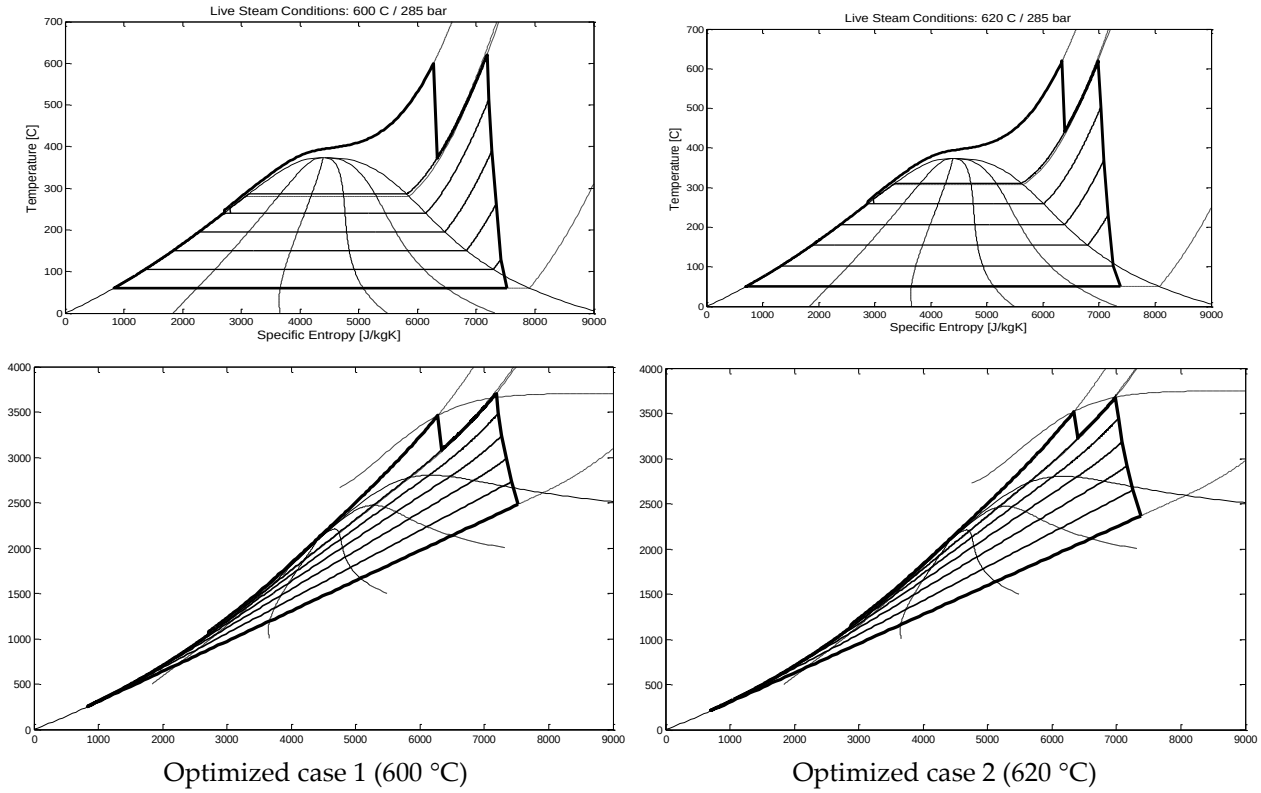


Figure 4. T-s (**top**) and h-s diagrams (**bottom**).

Figure 5 shows the detailed temperature evolution of the water-steam (blue line) and hot particles (red line) in the detailed heat exchanger network. As can be noticed, improved thermal performance can be achieved for the supercritical cycle scheme compared to similar subcritical cases [25]. This is based on the higher average temperature of the added heat and the single phase transition for the supercritical state.

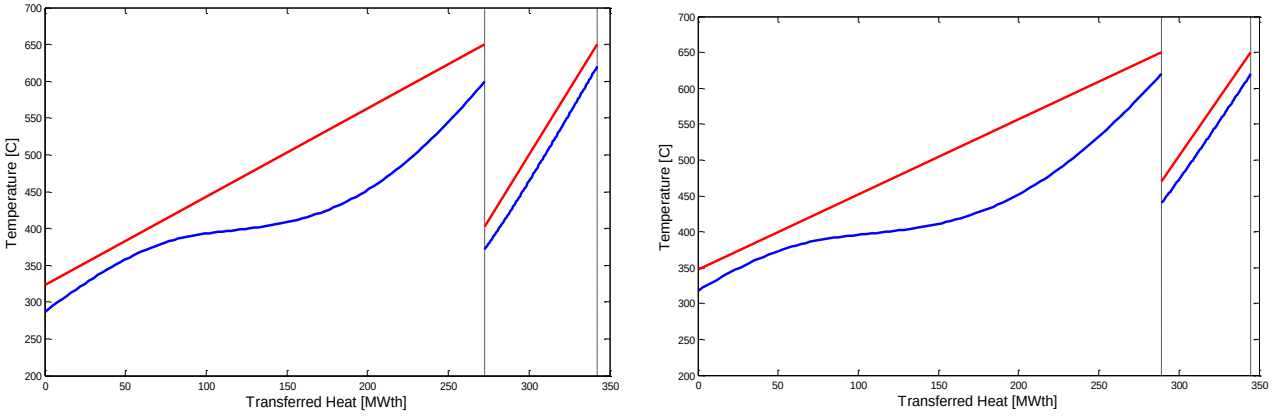


Figure 5. Steam generator temperature evolution (water-steam in blue and hot particles in red).

The average temperature is related to the heat input and the entropy gain; the higher the pressure, the higher the temperature of the plateau of the subcritical cycle (or the pseudo-plateau of a supercritical cycle). The second reason is as follows: the higher the pressure, the smaller the phase-change plateau, which is replaced by an s-shape profile when the cycle becomes supercritical (p > 221 bar). Consequently, the exergetic losses of the heat transfer between the primary fluids (combustion gas in a coal plant or particles in this case) are lower because the ΔT is lower.

Condensing Temperature Effect

Table 4 summarizes the power balance of the different power plant components for working conditions corresponding to optimized Case 2, where different condensing temperatures are considered. As can be observed, the lower the condensing temperature, the higher the power produced at the low-pressure turbine, as expected. However, the water inlet temperature at the steam generator is also lower, and for that, it requires higher added heat to reach the given superheated steam conditions (620 °C at 285 bar).

Table 4. Power consumption at different condensing temperatures.

Parameter	Unit	42 °C	50 °C	58 °C
Ambient temperature	°C	25	25	25
Condenser ΔT	°C	15	15	15
$Q_{steam\ generator}$	MW_{th}	311.15	277.45	279.40
$Q_{reheater}$	MW_{th}	59.54	53.31	53.90
Total heat addition	MW_{th}	370.69	330.76	333.30
$W_{turbine}$ HP	MW_e	44.90	40.00	40.24
$W_{turbine}$ LP	MW_e	142.42	123.81	121.47
Turbine power	MW_e	187.32	163.81	161.71
Circulating pump	MW_e	0.67	0.62	0.64
Feed-water pump	MW_e	5.34	4.74	4.76
Condenser pump	MW_e	2.70	0.49	0.28
Condenser fan	MW_e	24.20	4.47	2.62

As can be observed in Table 4 and Figure 6, the electric power consumed by the condenser fan rapidly increases as a function of the temperature (from 50 °C to 42 °C), which reduces the power cycle efficiency considerably.

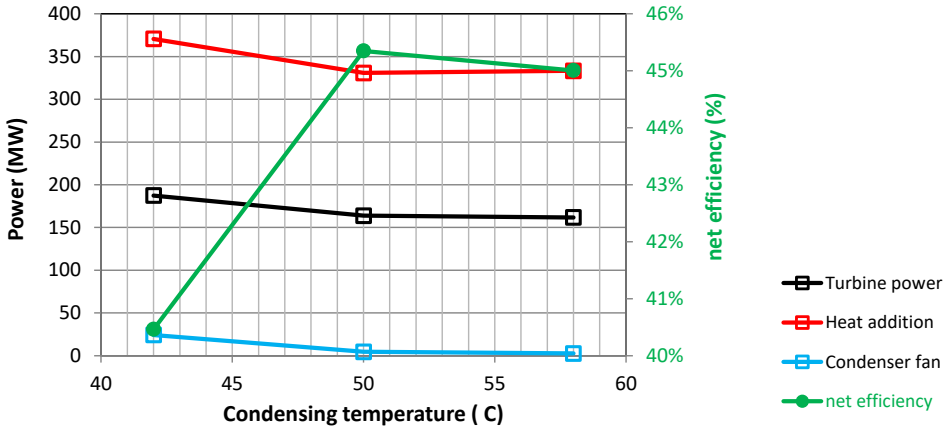


Figure 6. Condensing temperature effect on power block efficiency.

Summarizing, a net power cycle efficiency above 45% (as targeted in Table 1) can be achieved by considering the supercritical steam Rankine cycle coupled to a solar particle receiver working at 650 °C. The optimized power cycle configuration is based on 620 °C and 285 bar steam in a single reheated cycle with a 50 °C condensing temperature. Despite the higher gross efficiency found in Table 3 (close to 48%), the net cycle efficiency is limited to 45.35% due to the large parasitic losses introduced by the dry-condenser fan's power consumption and the high condensing temperature (50 °C). Commercial supercritical Rankine cycles in coal-fired power plants exhibit slightly higher net efficiencies (above 46%) [34] due to the wet-cooling system, which allows for lower condensing temperatures and lower parasitic power consumption.

3.2. Supercritical CO_2 Cycle (S-CO_2)

Figure 7 shows the plant layout of a recompression s-CO_2 power cycle coupled with a solar particle receiver. The recompression s-CO_2 plant layout was chosen due to its simplicity and reasonably good efficiency [21,35]. This cycle is highly recuperative and consists of a low-temperature (LTR) and high-temperature heat exchanger (HTR). The CO_2 mass split fraction that circulates through each compressor and recuperator is crucial for maximizing the power cycle efficiency [36]. As several researchers have discussed, optimal results are found for a split fraction around 0.25, depending on the recuperator efficiency and pinch point temperature [37]. This means that 25% of the total circulating mass flow is diverted to the recompression compressor (RC), while 75% of the mass flow is pumped by the main compressor (MC).

As has been stated by several researchers [36], the s-CO_2 power cycle efficiency is very sensitive to the working conditions, especially to the lowest temperature of the cycle (main compressor inlet temperature). This sensitivity is based on the CO_2 density and sudden changes in specific heat near the critical point (74 bar and 31 °C). In fact, near the critical point, CO_2 behaves as a liquid, and therefore, very low specific work is needed for compression (the compressor behaves as a pump). Nevertheless, as the compressor inlet temperature slightly increases above the critical temperature, the power required for compression rapidly increases (as happens with standard air Brayton cycles), which, in turn, reduces the power cycle efficiency.

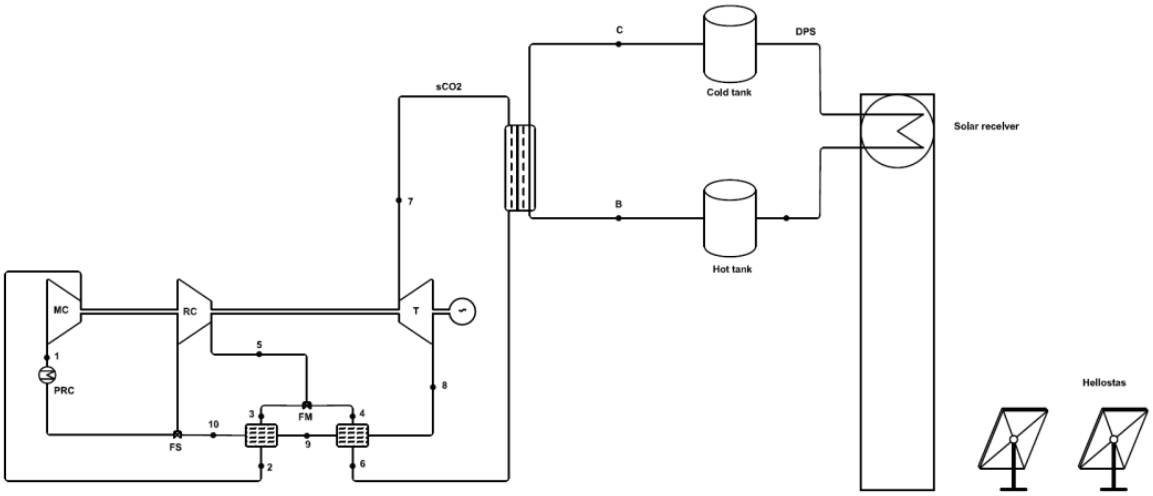


Figure 7. Recompression S-CO_2 cycle layout.

Despite the widespread research interest in this power cycle for electricity production, which is based on its promising cycle efficiency and very compact components, there are still many technical challenges to be solved for the commercial deployment of this cycle concept in the near future [38]. The main limitations are related to the need for special materials and sealings due to the corrosive nature of the working fluid, the very high working pressures (from 70 bar up to 300 bar) and the need for ensuring a compressor inlet temperature close to the critical one, which can limit power plant operations in arid areas. However, the adoption of certain dopants in the HTF instead of pure CO_2 can increase the fluid's critical temperature, allowing for a condensing cycle in a hot environment with an ambient temperature higher than 40 °C [39].

The working condition limits gathered in Table 5 were considered for power cycle simulations based on a thorough literature review [40] due to the lack of real data on commercial applications for electricity generation.

Table 5. S-CO_2 power cycle boundary conditions for simulations.

Parameter	Unit	Value
Main compressor inlet temperature	°C	33–40
Main compressor inlet pressure	bar	78
Turbine inlet temperature	°C	680–730
Upper pressure	bar	248
HT recuperator effectiveness	%	90–95
LT recuperator effectiveness	%	90–95
Turbine isentropic efficiency	%	92
Compressor isentropic efficiency	%	88

Figure 8 shows the temperature and enthalpy evolution of the S-CO_2 cycle for a main compressor inlet temperature (CIT) of 40 °C and a turbine inlet temperature of 680 °C and the nomenclature used in Figure 7.

Considering the impact of a low temperature (MC compressor inlet) and high temperature (turbine inlet) on s-CO_2 cycle performance, a sensitivity analysis was conducted considering two temperature levels for both the main compressor inlet (33 °C and 44 °C) and the turbine inlet (680 °C and 730 °C).

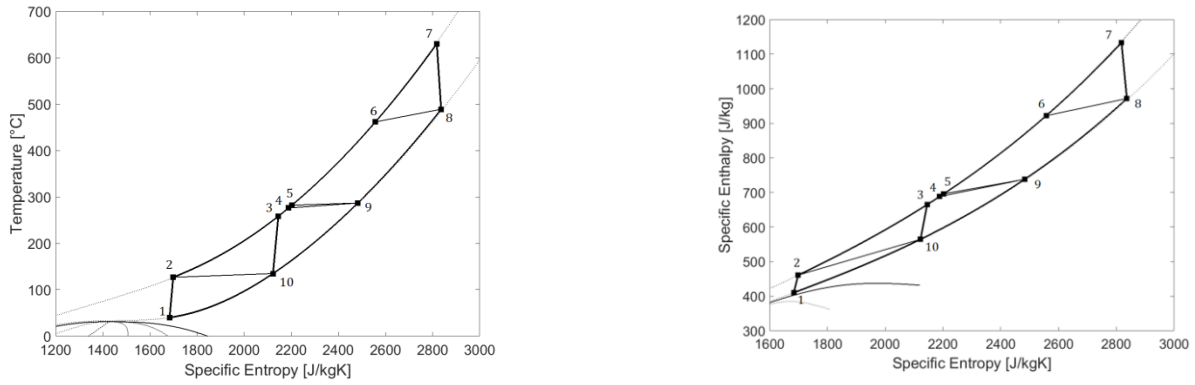


Figure 8. T-s (**left**) and h-s (**right**) diagrams for recompression S-CO_2 power cycle.

As can be observed in Table 6, there is an extreme impact on the power cycle efficiency as the compressor inlet temperature increases. As can be seen in Figure 9, the closer the compressor inlet temperature (T_{IC}) to the critical temperature (T_{crit}), the higher the power cycle efficiency. When the compressor inlet temperature increases to 2 °C above the critical point, the estimated power cycle efficiency is 52%. However, as the compressor inlet temperature increases to 13 °C above the critical point, the net cycle efficiency is drastically reduced to 42%. Practically, increasing the compressor inlet temperature by 1 °C reduces the power cycle efficiency by 1%. In the same graph, the turbine inlet temperature effect can be observed, where solid lines refer to a 680 °C turbine inlet temperature (TIT), while dashed lines refer to a 730 °C TIT. It can be summarized that increasing TIT by 50 °C represents a 1% improvement in the net cycle efficiency.

Table 6. Power cycle sensitivity analysis at cold and hot temperatures.

Parameter	Unit	Case 1	Case 2	Case 3	Case 4
Compressor inlet temperature	°C	33	40	33	40
Turbine inlet temperature	°C	680	680	730	730
LP compressor inlet pressure	bar	78	78	78	78
HP compressor outlet pressure	bar	248	248	248	248
LP compressor power consumption	MW_e	9.02	18.65	8.38	17.09
HP compressor power consumption	MW_e	7.91	12.26	7.35	11.24
Turbine power production	MW_e	67.94	81.98	66.76	79.40
Net power cycle power production	MW_e	50	50	50	50
S-CO_2 mass flow	kg/s	401.14	484.02	373.02	443.67
Cycle thermal efficiency	%	53.20	47.13	54.25	48.64
Net cycle efficiency	%	52.13	46.14	53.17	47.62

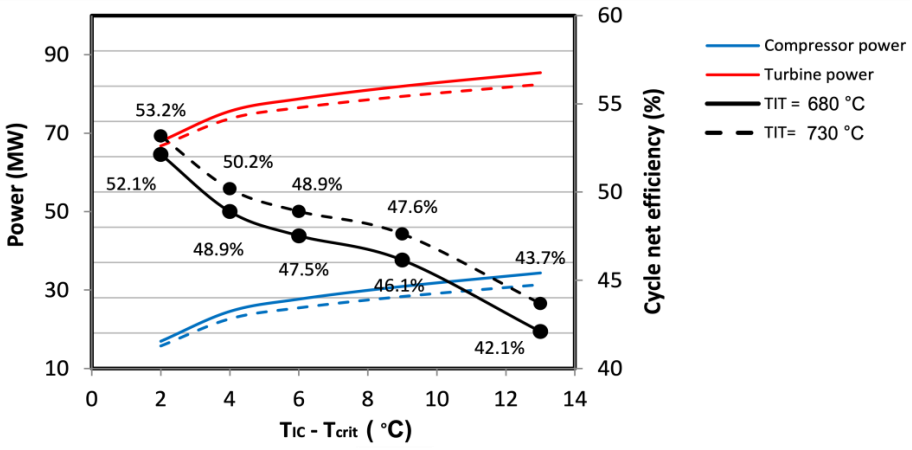
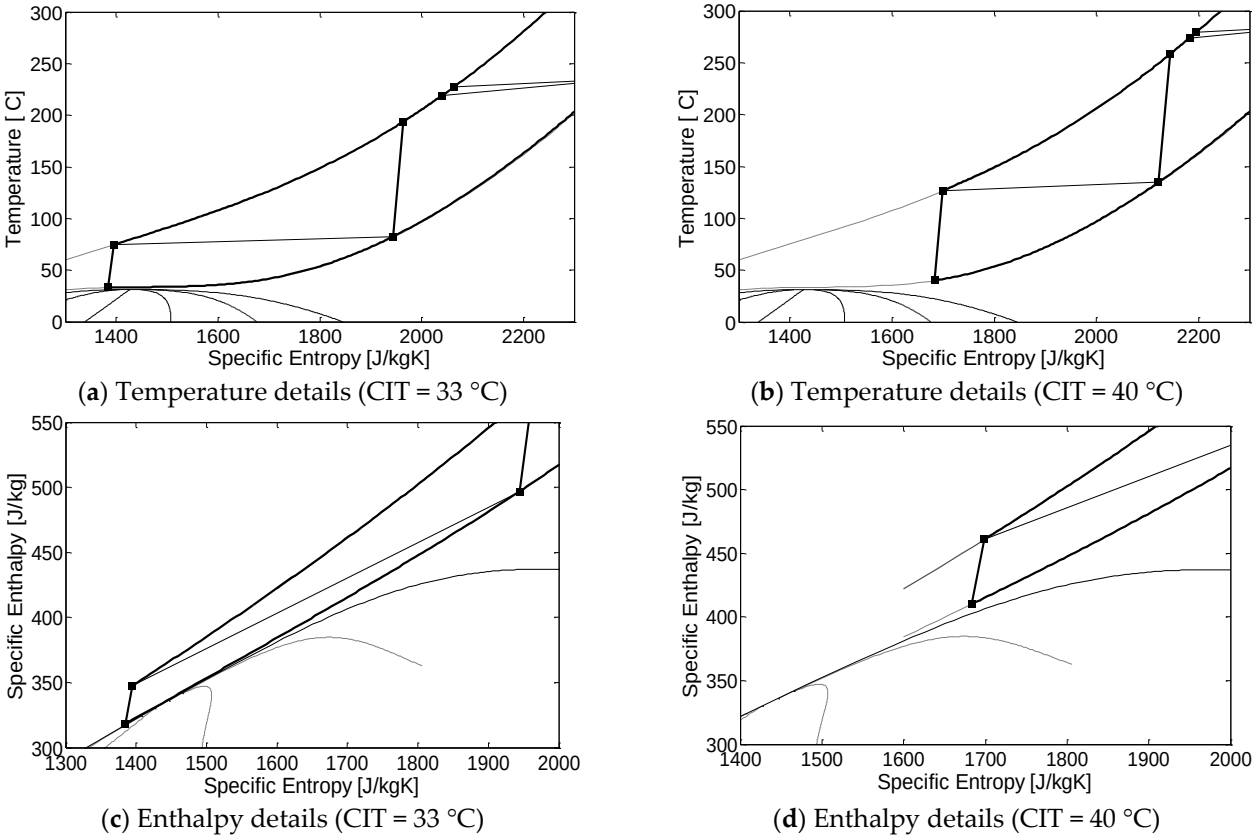


Figure 9. Power cycle sensitivity analysis at cold and hot temperatures.

The compressor inlet temperature effect can be observed in Figure 10, where enthalpy lines converge near the critical temperature, and hence, the absorbed power of the main compressor is significantly reduced.



(**a**) Temperature details (CIT = 33 °C)

(**b**) Temperature details (CIT = 40 °C)

(**c**) Enthalpy details (CIT = 33 °C)

(**d**) Enthalpy details (CIT = 40 °C)

Figure 10. Detailed figures showing the effect of compressor inlet temperature. Left figures show more detail on the compressor inlet points.

In Figures 9 and 10, it can be observed that there is a real need for reducing the compressor inlet state to as close as possible to the critical point conditions. Therefore, a wet-cooling condenser seems to be the most efficient option for this power cycle, mainly when coupled with CSP.

As can be noticed in Figure 11, the particle receiver efficiency is barely affected by the compressor inlet temperature. However, the efficiency of the power cycle is improved thanks to the temperature increase of 50 °C, which nevertheless causes an increase in thermal losses in the efficiency of the solar receiver. Therefore, it can be concluded that there is no significant improvement in the sun-to-electricity efficiency by increasing TIT up to 730 °C.

The s-CO_2 power cycle showed promising theoretical results, gaining a net cycle efficiency of over 50% (as was targeted) for a moderate temperature level at the turbine inlet. Nevertheless, it should be kept in mind that lowering the compressor inlet temperature closer to the critical conditions will be crucial for meeting the high-efficiency expectation. The dry cooling solution for pure CO_2 is not recommended due to the cycle sensitivity to the compressor inlet temperature.

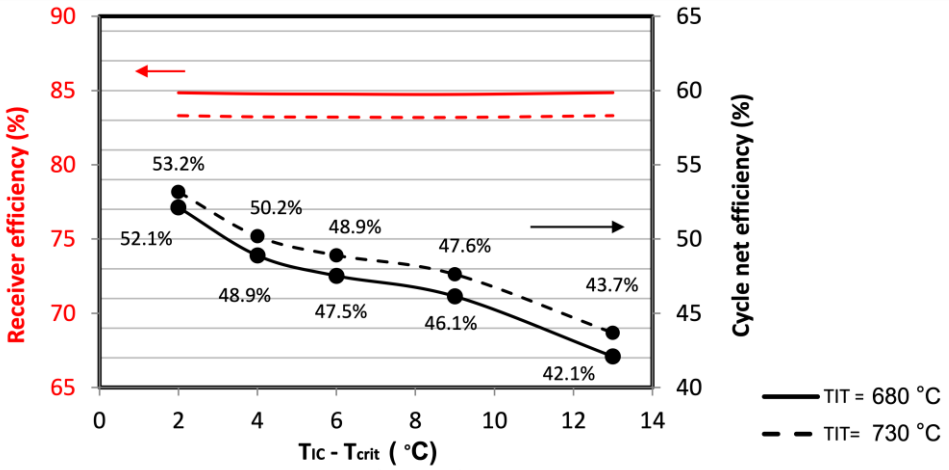


Figure 11. Receiver efficiency (red solid and dashed lines) and cycle net efficiency (black solid and dashed lines) as a function of the compressor inlet temperature and turbine inlet temperature.

3.3. Integrated Solar Combined Cycle (ISCC)

In this section, the optimization of the ISCC layout is addressed, aimed at maximizing the efficiency of the power block. Different working conditions for the topping and bottoming power cycles (working pressures, maximum temperatures, cycle arrangement, etc.) were investigated considering a nameplate power of 150 MW_e and a receiver outlet DPS temperature of 800 °C. The dry condenser configuration was considered for dry climate scenarios. The components' efficiency and losses in Table 7 were considered [15].

Table 7. Power plant components' modelled efficiency and losses.

Parameter	Unit	Value
Topping cycle	-	-
Compressor isentropic efficiency	%	88
Main turbine isentropic efficiency	%	91
Reheating turbine isentropic efficiency	%	91
Temperature losses at turbine inlet	°C	20
Pressure losses at auxiliary burner	mbar	30
Bottoming cycle	-	-
Pump efficiency	%	85
Main turbine isentropic efficiency	%	88
Reheating turbine isentropic efficiency	%	91
Reheating pressure losses	mbar	5000
Condenser ΔT (dry)	°C	10
Condenser ΔT (wet)	°C	10
Ambient temperature	°C	25
Fan mechanical efficiency	%	75

Several modifications were applied to the ISCC plant layout presented in previous works [15] in order to increase the net cycle efficiency. The optimized power cycle architecture is shown in Figure 12, where the modifications consist of an uncooled and unfired double-reheated topping Brayton cycle and a two-pressure subcritical Rankine cycle without steam extraction for the bottoming cycle.

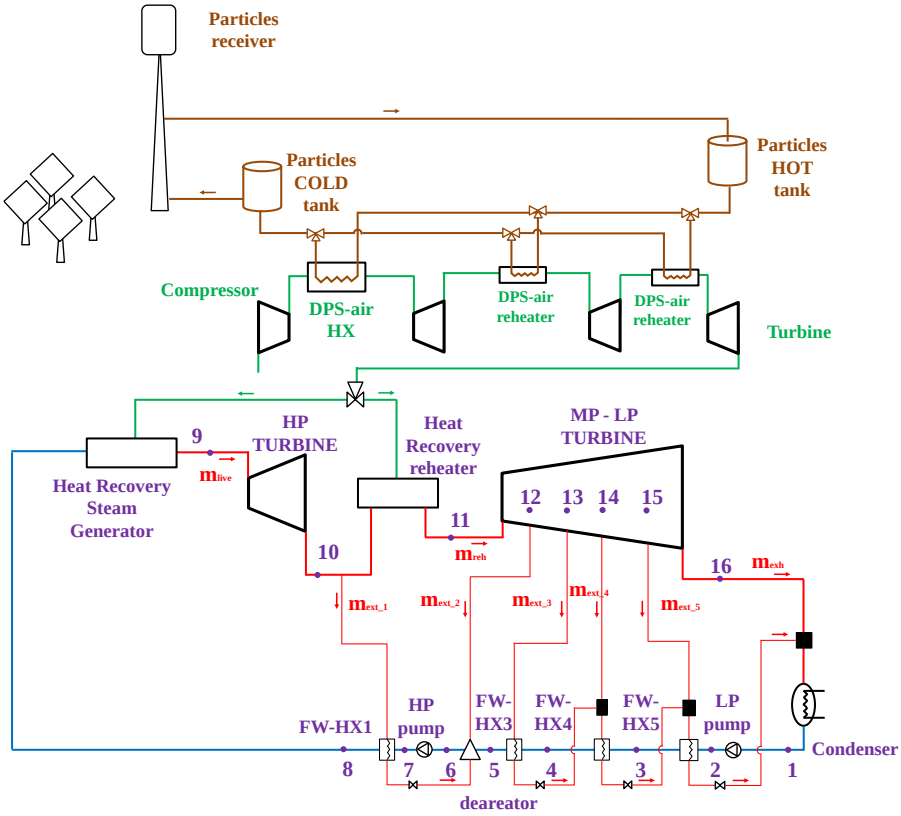


Figure 12. Integrated solar combined power cycle: HX (heat exchanger), MP (medium pressure), LP (Low Pressure), FW (Feedwater preheating chain).

As can be observed in Figure 13, the Brayton double-reheating cycle allows an increase in the added heat's average temperature, which is beneficial for the power cycle efficiency according to the second law of thermodynamics. The double-reheating process also allows for increasing the pressure ratio of the Brayton cycle, which translates into a higher average temperature of the added heat and a higher temperature at the end of the compression process (point 4) and, hence, a significant reduction in external heat addition. Despite the higher power consumption in the compression process, an improvement in the net cycle efficiency is expected. Furthermore, double turbine reheating allows for increasing the power plant efficiency when TIT is limited, as happens in this case due to the metallurgical limit of the turbine blade material for uncooled vanes. Table 8 lists the process and the description of the double-reheating topping Brayton cycle in Figure 13.

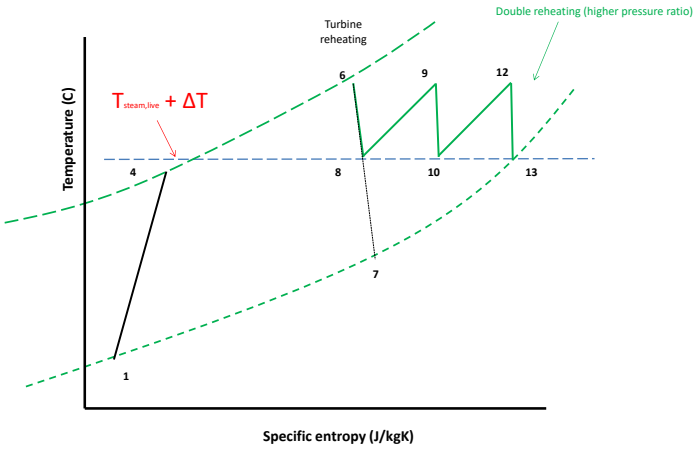


Figure 13. Double-reheating topping Brayton cycle.

Table 8. Process description of the T-s diagram in Figure 13.

Process	Description
$1 \rightarrow 4$	Uncooled compression
$4 \rightarrow 6$	External heat addition (fluidized-bed heat exchanger)
$6 \rightarrow 68$	HP turbine expansion
$8 \rightarrow 9$	MP reheating (fluidized-bed heat exchanger)
$9 \rightarrow 10$	MP turbine expansion
$10 \rightarrow 12$	LP reheating (fluidized-bed heat exchanger)
$12 \rightarrow 13$	LP turbine expansion
$6 \rightarrow 7$	Single-Brayton-cycle turbine expansion (non-reheated cycle)

Table 9 lists the ISCC working parameters for the reference case [15] and the optimal solution. As can be observed, a net cycle efficiency of over 45% can be achieved with the double-reheating process in the turbine using only solar thermal energy from the particle receiver and a maximum TIT of 780 °C compared to the high temperature of 1100 °C.

Table 9. Combined cycle refinement (double reheating).

Parameter	Unit	Reference Case	Optimized Case
Receiver outlet temperature	°C	650	800
Topping cycle (Brayton)			
Turbine inlet temperature	°C	1100	780
Pressure ratio	-	5	21
Auxiliary back-up burner	-	yes	No
Compressor intercooling	-	yes	No
Turbine reheating	-	no	Double
Required solar thermal power	MW_{th}	164.84	329.9
Required burner thermal power	MW_{th}	187.26	0
Net power	MW_e	87.87	90.8
Bottoming cycle (Rankine)			
Superheated steam temperature	°C	610	540
Reheated steam temperature	°C	600	530
Steam condensing temperature	°C	50	45
Superheated steam pressure	bar	180	160
Reheated steam pressure	bar	25	30
Steam extractions	-	yes	no
Superheated steam mass flow	kg/s	48.64	45.58
Reheated steam mass flow	kg/s	45.50	45.58
Condenser mass flow	kg/s	43.08	45.58
Preheating + evaporating + superheating power	MW_{th}	125.3	115.01
Reheating power	MW_{th}	26.8	22.5
Net power	MW_e	62.0	59.0
Power plant			
Nameplate production	MW_e	150	150
Solar share	%	46.82	100
Net efficiency	%	42.57	45.23

To reduce exergy destruction in the solar plant, it was decided that particle heat addition would take place at the same temperature level. In other words, the temperatures of working points 4, 8 and 10 (from Figure 13) should be very similar.

The higher the TIT of the topping cycle, the higher the net power cycle efficiency. Figure 14 shows ISCC's net efficiency for the double-reheating configuration of the topping cycle at higher TIT; in these cases, the use of a back-up gas burner is assumed to increase the temperature level. The working conditions for the bottoming Rankine cycle (of ISCC) are kept the same as shown for the optimized case in Table 10. As can be noticed, the higher the TIT, the higher the ISCC efficiency. However, the solar contribution drastically decreases from 100% (pure solar mode) to below 50%, as can be observed in Table 10.

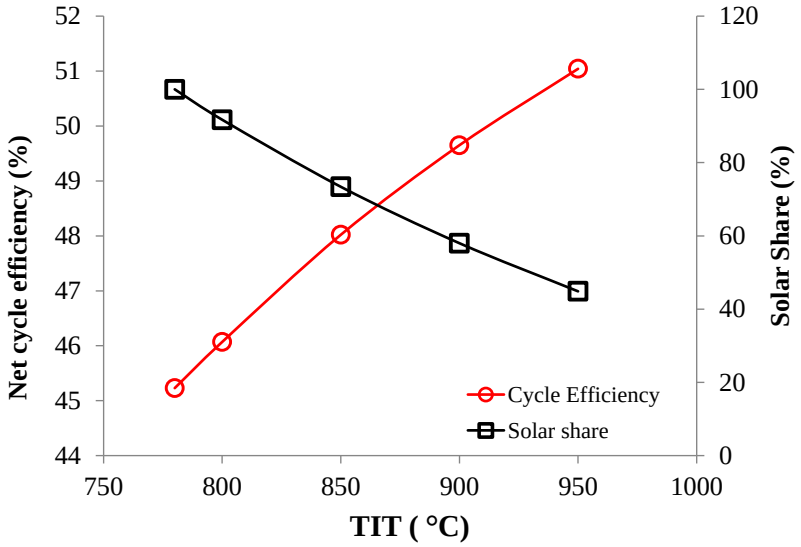


Figure 14. Effect of TIT on combined cycle efficiency.

Table 10. Effect of TIT on combined cycle efficiency.

Parameter	Unit	Case 1	Case 2	Case 3	Case 4	Case 5
Turbine inlet temperature	°C	780	800	850	900	950
Receiver outlet temperature	°C	800	800	800	800	800
Topping cycle (Brayton)	-	-	-	-	-	-
Auxiliary back-up burner	-	no	yes	yes	yes	yes
Pressure ratio	-	21	21	21	21	21
Required solar power	MW_{th}	329.9	299.1	229.2	175.3	132.0
Required burner power	MW_{th}	0	27.1	83.1	127.0	162.3
Net power	MW_e	90.8	91.3	91.5	91.8	92.0
Bottoming cycle (Rankine)	-					
Steam mass flow	kg/s	45.58	45.58	45.20	45.04	44.96
Net power	MW_e	59.0	59.0	58.5	58.3	58.2
Power plant	-	-	-	-	-	-
Nameplate production	MW_e	149.8	150.3	150.0	150.0	150.2
Solar share	%	100	91.7	73.4	58.0	44.86
Net efficiency	%	45.23	46.07	48.02	49.65	51.04

4. Discussion

Regarding the power plant performance comparison, the net efficiency gives a direct indication regarding the best choice. Table 11 lists the net cycle efficiency, the HTF turbine inlet temperature and some remarks regarding the configuration for each cycle layout and for the related optimized case.

Table 11. Main information of the plant comparison.

Parameter	Unit	S-Steam	S-CO_2	ISCC
Net cycle efficiency	%	45.35	53.17	45.23
HTF turbine inlet temperature	°C	620	730	780
Remarks	-	High parasitic losses	Needs wet cooling, sensitive to CIT	Solar receiver re-design

Concerning the supercritical steam cycle, a net power cycle efficiency above 45% can be achieved (gross power cycle efficiency of almost 48%) near the set target; despite this, there are high parasitic losses due to the power consumption of the fan of the dry-cooling system.

The recompression S-CO_2 cycle showed an efficiency of 53.17%, above the targeted value of 50%, obtained at moderate TIT (680 °C to 730 °C). However, such high efficiencies

cannot be achieved without wet cooling. Furthermore, cycle efficiency is very sensitive to CIT (the closer the temperature to the critical point, the higher the efficiency).

Finally, the net efficiency gained 1% on the power block by increasing TIT from 680 °C to 730 °C; despite this, the thermal efficiency of the receiver decreased by 1%.

The integrated solar combined cycle showed a net cycle efficiency above 45% for the pure solar combined cycle gas turbine, with an uncooled, double-reheating configuration at a TIT of 780 °C. The most efficient Brayton cycle has equal pressure ratios across all turbines. Furthermore, setting these pressure ratios for equal air temperatures at every DPS-HX inlet may simplify the DPS-HX particle-side layout. The best ISCC layout exhibits net power cycle efficiency above 45%. The targeted efficiency expectations of at least 50% for the ISCC were not achieved due to the very low TIT (780 °C) compared to the working conditions of actual and very efficient combined power plants. If the particle receiver were to be re-designed to allow a TIT above 800 °C, a net cycle efficiency above 50% can be achieved.

5. Conclusions

In this paper, three potential power cycles coupled with DPS technology are screened and compared for electricity production. The studied cycles all have the potential to reach very high efficiencies at temperature levels compatible with DPS in the solar-only configuration. In each power cycle, the working conditions were determined to maximize the net efficiency and to reach the CSP Gen3 efficiency target of 50%. The main finding of this exploratory research indicates that the S-CO_2 power cycle can reach an efficiency of 53.17%, displaying a strong potential for future applications in CSP, particularly when coupled with DPS at a moderate temperature level of the turbine inlet. Despite this, a low compressor inlet temperature, closer to critical conditions, is necessary for achieving high-efficiency expectations. ISCC showed a net cycle efficiency above 45% for the pure solar combined cycle gas turbine with an uncooled, double-reheating configuration; however, the low TIT limits its efficiency. Finally, the S-Steam power cycle displayed a higher gross efficiency, close to 48%, but the net cycle efficiency is limited to 45.35% due to the large parasitic losses caused by the dry-condenser fan's power consumption and high condensing temperature. Further research will be conducted on yearly simulations and the part-load operations related to the proposed power cycles. Finally, a detailed economic assessment will be carried out to establish the advantages and disadvantages of each system analyzed.

Author Contributions: Conceptualization, M.A.R.-B. and F.R.; methodology, M.A.R.-B.; software, M.A.R.-B.; validation, M.A.R.-B. and F.R.; formal analysis, M.A.R.-B. and F.R.; investigation, M.A.R.-B. and F.R.; writing—original draft preparation, M.A.R.-B. and F.R.; writing—review and editing, M.A.R.-B. and F.R. All authors have read and agreed to the published version of the manuscript.

Funding: This research received no external funding.

Data Availability Statement: Not applicable.

Conflicts of Interest: The authors declare no conflict of interest.

References

1. Shahabuddin, M.; Alim, M.A.; Alam, T.; Mofijur, M.; Ahmed, S.F.; Perkins, G. A Critical Review on the Development and Challenges of Concentrated Solar Power Technologies. *Sustain. Energy Technol. Assess.* **2021**, *47*, 101434. [CrossRef]
2. Morrone, P.; Algieri, A.; Castiglione, T.; Perrone, D.; Bova, S. Investigation of the Energy Performance of Multi-Source Integrated CHP Systems for Small-Scale Applications. In *AIP Conference Proceedings*; AIP Publishing LLC: Melville, NY, USA, 2019; Volume 2191, p. 20098. [CrossRef]
3. European Commission. Energy Roadmap 2050. 2012. Available online: https://op.europa.eu/en/publication-detail/-/publication/874c6c35-cbee-4987-b9aa-a0c860428ce0/language-en/format-PDF (accessed on 1 July 2022).
4. Lovegrove, K.; Stein, W. *Concentrating Solar Power Technology: Principles, Developments and Applications*; Elsevier: Amsterdam, The Netherlands, 2012; ISBN 978-1-84569-769-3.
5. Zhang, H.L.; Baeyens, J.; Degrève, J.; Cacères, G. Concentrated Solar Power Plants: Review and Design Methodology. *Renew. Sustain. Energy Rev.* **2013**, *22*, 466–481. [CrossRef]

6. CSP Alliance. The Economic and Reliability Benefits of CSP with Thermal Energy Storage: Recent Studies and Research Needs. 2012, Volume 1. Available online: https://inship.psa.es/docs/TES%204%20the_economic_and_reliability_benefits_of_csp_with_thermal_storage_2014_09_09_final.pdf (accessed on 1 July 2022).
7. Martín, H.; de la Hoz, J.; Velasco, G.; Castilla, M.; García de Vicuña, J.L. Promotion of Concentrating Solar Thermal Power (CSP) in Spain: Performance Analysis of the Period 1998–2013. *Renew. Sustain. Energy Rev.* **2015**, *50*, 1052–1068. [CrossRef]
8. Kuravi, S.; Trahan, J.; Goswami, D.Y.; Rahman, M.M.; Stefanakos, E.K. Thermal Energy Storage Technologies and Systems for Concentrating Solar Power Plants. *Prog. Energy Combust. Sci.* **2013**, *39*, 285–319. [CrossRef]
9. Ortega, J.I.; Burgaleta, J.I.; Téllez, F.M. Central Receiver System Solar Power Plant Using Molten Salt as Heat Transfer Fluid. *J. Sol. Energy Eng.* **2008**, *130*, 024501. [CrossRef]
10. Montes, M.J.; Abánades, A.; Martínez-Val, J.M. Performance of a Direct Steam Generation Solar Thermal Power Plant for Electricity Production as a Function of the Solar Multiple. *Sol. Energy* **2009**, *83*, 679–689. [CrossRef]
11. Laing, D.; Bahl, C.; Bauer, T.; Lehmann, D.; Steinmann, W.-D. Thermal Energy Storage for Direct Steam Generation. *Sol. Energy* **2011**, *85*, 627–633. [CrossRef]
12. Giuliano, S.; Buck, R.; Eguiguren, S. Analysis of Solar-Thermal Power Plants with Thermal Energy Storage and Solar-Hybrid Operation Strategy. *J. Sol. Energy Eng.* **2011**, *133*, 031007. [CrossRef]
13. Benoit, H.; Spreafico, L.; Gauthier, D.; Flamant, G. Review of Heat Transfer Fluids in Tube-Receivers Used in Concentrating Solar Thermal Systems: Properties and Heat Transfer Coefficients. *Renew. Sustain. Energy Rev.* **2016**, *55*, 298–315. [CrossRef]
14. Mehos, M.; Turchi, C.; Vidal, J.; Wagner, M.; Ma, Z.; Ho, C.; Kolb, W.; Andraka, C.; Kruizenga, A. Concentrating Solar Power Gen3 Demonstration Roadmap. In *Concentrating Solar Power Gen3 Demonstration Roadmap*; Office of Scientific and Technical Information (OSTI): Golden, CO, USA, 2017.
15. Reyes-Belmonte, M.A.; Sebastián, A.; González-Aguilar, J.; Romero, M. Performance Comparison of Different Thermodynamic Cycles for an Innovative Central Receiver Solar Power Plant. In *AIP Conference Proceedings*; AIP Publishing LLC: Melville, NY, USA, 2017; Volume 1850. [CrossRef]
16. Turchi, C.; Gage, S.; Martinek, J.; Jape, S.; Armijo, K.; Coventry, J.; Pye, J.; Asselineau, C.-A.; Venn, F.; Logie, W.; et al. CSP Gen3: Liquid-Phase Pathway to SunShot Golden, CO: National Renewable Energy Laboratory. NREL/TP-5700-79323. 2021. Available online: https://www.nrel.gov/docs/fy21osti/79323.pdf (accessed on 1 July 2022).
17. Rovense, F.; Perez, M.S.; Amelio, M.; Ferraro, V.; Scornaienchi, N.M. Feasibility Analysis of a Solar Field for a Closed Unfired Joule-Brayton Cycle. *Int. J. Heat Technol.* **2017**, *35*, S166–S171. [CrossRef]
18. Rovense, F.; Reyes-Belmonte, M.A.; González-Aguilar, J.; Amelio, M.; Bova, S.; Romero, M. Flexible Electricity Dispatch for CSP Plant Using Un-Fired Closed Air Brayton Cycle with Particles Based Thermal Energy Storage System. *Energy* **2019**, *173*, 971–984. [CrossRef]
19. Rovense, F.; Reyes-Belmonte, M.A.; González-Aguilar, J.; Amelio, M.; Bova, S.; Romero, M. Application of Un-Fired Closed Brayton Cycle with Mass Flow Regulation and Particles-Based Thermal Energy Storage Systems for CSP. *AIP Conf. Proc.* **2019**, *2126*, 030047. [CrossRef]
20. Spelling, J.; Gallo, A.; Romero, M.; González-Aguilar, J. A High-Efficiency Solar Thermal Power Plant Using a Dense Particle Suspension as the Heat Transfer Fluid. *Energy Procedia* **2015**, *69*, 1160–1170. [CrossRef]
21. Chen, R.; Romero, M.; González-Aguilar, J.; Rovense, F.; Rao, Z.; Liao, S. Design and Off-Design Performance Comparison of Supercritical Carbon Dioxide Brayton Cycles for Particle-Based High Temperature Concentrating Solar Power Plants. *Energy Convers. Manag.* **2021**, *232*, 113870. [CrossRef]
22. Chen, R.; Romero, M.; González-Aguilar, J.; Rovense, F.; Rao, Z.; Liao, S. Optical and Thermal Integration Analysis of Supercritical CO_2 Brayton Cycles with a Particle-Based Solar Thermal Plant Based on Annual Performance. *Renew. Energy* **2022**, *189*, 164–179. [CrossRef]
23. Rovense, F.; Reyes-Belmonte, M.Á.; Romero, M.; González-Aguilar, J. Thermo-Economic Analysis of a Particle-Based Multi-Tower Solar Power Plant Using Unfired Combined Cycle for Evening Peak Power Generation. *Energy* **2022**, *240*, 122798. [CrossRef]
24. CSP2: Concentrated Solar Power in Particles. Available online: http://www.csp2-project.eu (accessed on 29 September 2022).
25. Reyes-Belmonte, M.A.; Sebastián, A.; Spelling, J.; Romero, M.; Gonzalez-Aguilar, J. Annual Performance of Subcritical Rankine Cycle Coupled with an Innovative Particle Receiver Solar Power Plant. *Renew. Energy* **2019**, *130*, 786–795. [CrossRef]
26. Reyes-Belmonte, M.A.; Gómez-García, F.; González-Aguilar, J.; Romero, M.; Benoit, H.; Flamant, G. Heat Exchanger Modelling in Central Receiver Solar Power Plant Using Dense Particle Suspension. *AIP Conf. Proc.* **2017**, *1850*, 030042. [CrossRef]
27. Gallo, A.; Spelling, J.; Romero, M.; González-Aguilar, J. Preliminary Design and Performance Analysis of a Multi-Megawatt Scale Dense Particle Suspension Receiver. *Energy Procedia* **2015**, *69*, 388–397. [CrossRef]
28. Gomez-Garcia, F.; Gauthier, D.; Flamant, G. Design and Performance of a Multistage Fluidised Bed Heat Exchanger for Particle-Receiver Solar Power Plants with Storage. *Appl. Energy* **2017**, *190*, 510–523. [CrossRef]
29. Reyes-Belmonte, M.A.; Díaz, E.; Romero, M.; González-Aguilar, J. Particles-Based Thermal Energy Storage Systems for Concentrated Solar Power. In *AIP Conference Proceedings*; AIP Publishing LLC: Melville, NY, USA, 2018; Volume 79, p. 210013.
30. Ho, C.K. A Review of High-Temperature Particle Receivers for Concentrating Solar Power. *Appl. Therm. Eng.* **2016**, *109*, 958–969. [CrossRef]
31. Reyes-Belmonte, M.A.; Pino, F.J.; Romero, M.; Suarez, C.; González-Aguilar, J.; Guerra, J. Optimization of an Integrated Solar Combined Cycle. *AIP Conf. Proc.* **2018**, *2033*, 210012. [CrossRef]

32. Lee, J.J.; Kang, S.Y.; Kim, T.S.; Byun, S.S. Thermo-Economic Analysis on the Impact of Improving Inter-Stage Packing Seals in a 500 MW Class Supercritical Steam Turbine Power Plant. *Appl. Therm. Eng.* **2017**, *121*, 974–983. [CrossRef]
33. Silva-Pérez, M.A. *Solar Power Towers Using Supercritical CO_2 and Supercritical Steam Cycles, and Decoupled Combined Cycles*; Elsevier Ltd.: Amsterdam, The Netherlands, 2017; ISBN 9780081005170.
34. Tumanovskii, A.G.; Shvarts, A.L.; Somova, E.V.; Verbovetskii, E.K.; Avrutskii, G.D.; Ermakova, S.V.; Kalugin, R.N.; Lazarev, M.V. Review of the Coal-Fired, over-Supercritical and Ultra-Supercritical Steam Power Plants. *Therm. Eng.* **2017**, *64*, 83–96. [CrossRef]
35. Crespi, F.; Gavagnin, G.; Sánchez, D.; Martínez, G.S. Supercritical Carbon Dioxide Cycles for Power Generation: A Review. *Appl. Energy* **2017**, *195*, 152–183. [CrossRef]
36. Reyes-Belmonte, M.A.; Sebastián, A.; Romero, M.; González-Aguilar, J. Optimization of a Recompression Supercritical Carbon Dioxide Cycle for an Innovative Central Receiver Solar Power Plant. *Energy* **2016**, *112*, 17–27. [CrossRef]
37. Luu, M.T.; Milani, D.; McNaughton, R.; Abbas, A. Analysis for Flexible Operation of Supercritical CO_2 Brayton Cycle Integrated with Solar Thermal Systems. *Energy* **2017**, *124*, 752–771. [CrossRef]
38. Reyes-Belmonte, M.A.; Guédez, R.; Montes, M.J. Bibliometric Analysis on Supercritical CO_2 Power Cycles for Concentrating Solar Power Applications. *Entropy* **2021**, *23*, 1289. [CrossRef]
39. Di Marcoberardino, G.; Morosini, E.; Di Bona, D.; Chiesa, P.; Invernizzi, C.; Iora, P.; Manzolini, G. Experimental Characterisation of CO_2 + C_6F_6 Mixture: Thermal Stability and Vapour Liquid Equilibrium Test for Its Application in Transcritical Power Cycle. *Appl. Therm. Eng.* **2022**, *212*, 118520. [CrossRef]
40. Liu, Y.; Wang, Y.; Huang, D. Supercritical CO_2 Brayton Cycle: A State-of-the-Art Review. *Energy* **2019**, *189*, 115900. [CrossRef]